Phys. Lett. B 879 (2026) 140614

Contents lists available at ScienceDirect

Physics Letters B

journal homepage: www.elsevier.com/locate/physletb

Letter

Role of shell effects on producing neutron-rich nuclei in the $N = 126$ region via multinucleon transfer reactions

F. C. Dai [a], P. W. Wen [b,*], C. J. Lin [b,c,*], J. J. Liu [a], X. X. Xu [a,d,e,*], K. L. Wang [a], Y. D. Chen [a,d], H. L. Yang [a,f]

[a] State Key Laboratory of Heavy Ion Science and Technology, Institute of Modern Physics, Chinese Academy of Sciences, Lanzhou, 730000, China
[b] China Institute of Atomic Energy, Beijing, 102413, China
[c] College of Physics and Technology, Guangxi Normal University, Guilin, 541004, China
[d] University of Chinese Academy of Sciences, Beijing, 100049, China
[e] Advanced Energy Science and Technology Guangdong Laboratory, Huizhou, 516003, China
[f] Key Laboratory of Magnetism and Magnetic Functional Materials, Lanzhou University, Lanzhou, 730000, China

A R T I C L E I N F O

Editor: Baha Balantekin

Keywords:
Multinucleon transfer reaction
CLIM-H model
$N = 126$ neutron-rich nuclei
Langevin dynamics
Master equation

A B S T R A C T

Neutron-rich nuclei near the $N = 126$ shell closure are vital for r-process nucleosynthesis but remain challenging to produce. Multinucleon transfer reactions offer a promising route. We investigate the role of shell effects in such processes by extending the CLIM-H model with a deformation-dependent mass formula and a scaling factor a that linearly adjusts the shell-correction strength. Calculations for ^{136}Xe on ^{208}Pb, ^{204}Hg, and ^{208}Hg targets reveal a dual role: shell effects enhance few-nucleon transfers near the entrance channel but strongly suppress fragments requiring the transfer of many nucleons, most severely for the doubly magic ^{208}Pb. This suppression stems from the cumulative transfer probabilities and is aggravated by lower survival after deexcitation. Thus, optimal production of exotic $N = 126$ nuclei requires avoiding strongly shell-closed collision partners at $N = 126$, as exemplified by doubly magic ^{208}Pb. We propose ^{238}U + ^{204}Hg at $E_{\text{c.m.}} \simeq 1.45\ V_B$ as a superior system, predicting significantly enhanced yields.

1. Introduction

Neutron-rich nuclei near the $N = 126$ shell closure are of fundamental importance in nuclear physics and astrophysics [1–3]. As the nuclei at the third waiting point of the rapid neutron capture process (r-process), they govern the formation of the pronounced $A \sim 195$ peak in the solar abundance pattern [4–6]. Consequently, their nuclear properties, such as masses [7,8], half-lives [9,10], and single-particle levels near the Fermi surface [11], serve as essential inputs for constraining the extreme conditions of r-process sites, such as neutron-star mergers [12].

Producing these nuclei, however, remains a significant experimental challenge. Conventional methods such as fusion-evaporation, fission, and projectile fragmentation (PF) struggle to efficiently access this region due to a combination of inherently low cross sections and the production of residues away from the neutron-rich side of stability [13,14].

Against this backdrop, multinucleon transfer (MNT) reactions have emerged as a viable approach to this region [15–17]. Pioneering experiments with ^{136}Xe + ^{198}Pt demonstrated enhanced production of neutron-rich $N = 126$ isotones compared to PF [18]. Subsequent studies revealed that heavier projectiles (e.g., ^{209}Bi + ^{238}U [19]) transfer more nucleons, produce heavier fragments, and yield significantly lower excitation energies than lighter systems (e.g., ^{136}Xe + ^{238}U [20]). Meanwhile, systematic investigations with Pb/Bi targets have mapped cross-section systematics for proton transfer up to $+8p$. Comparison with actinide-target data shows that these trends extend consistently across the same proton transfer channels [21]. Despite these advances, the underlying mechanisms governing MNT processes, particularly how shell effects influence the interplay between nucleon transfer and energy dissipation, remain not fully understood.

On the theoretical side, MNT dynamics have been studied using various approaches, including the Langevin dynamics [22,23], the DNS (dinuclear system) model [24–26], other transport equations [27,28], and microscopic methods such as time-dependent Hartree-Fock [29,30], stochastic mean-field theory [31], and time-dependent covariant density functional theory [32]. While these models have incorporated shell effects to some extent, a comprehensive and dynamic understanding of how shell effects influence fragment distributions in MNT reactions is still lacking. This gap motivates the present work.

To investigate the influence of the microscopic shell effect on MNT processes, reactions at energies near the Coulomb barrier are

* Corresponding authors.
E-mail addresses: wenpeiwei@ciae.ac.cn (P.W. Wen), cjlin@ciae.ac.cn (C.J. Lin), xinxing@impcas.ac.cn (X.X. Xu).

https://doi.org/10.1016/j.physletb.2026.140614
Received 10 April 2026; Received in revised form 1 June 2026; Accepted 2 June 2026
Available online 4 June 2026

particularly suitable. In such near-barrier collisions, the total excitation energy of the system is relatively low, ensuring that shell corrections remain significant throughout the interaction and can thus effectively influence the nucleon exchange process. Consequently, the shell effect of the collision partners is a key factor determining the efficiency of populating neutron-rich regions far from stability, as suggested by earlier studies of deep-inelastic collisions [33–36]. It is therefore essential to systematically investigate how shell effects shape the dynamics of near-barrier MNT reactions, both to advance theoretical understanding of these processes and to inform the optimal projectile-target combinations for synthesizing specific neutron-rich isotopes.

The recently developed reaction model, named Coupling the Langevin dynamics Iteratively with the Master equation based on the HICOL model (CLIM-H) [37], provides a powerful approach for such studies. Central to CLIM-H is the self-consistent coupling between the master equation, which governs the evolution of the fragment's proton and neutron numbers, and the Langevin dynamics, which drives the collective coordinates. These two components mutually influence each other throughout the reaction. This scheme naturally bridges macroscopic dynamics and microscopic stochasticity.

The CLIM-H model has been successfully applied to describe MNT dynamics for various systems, reproducing the overall trends of fragment distributions [37,38]. However, while the model captures the macroscopic features, it remains limited in describing the detailed isotopic distributions, particularly in regions where shell effects are expected to play a crucial role.

This limitation stems from the model's treatment of nuclear masses: currently taken from AME2020 [39], they lack a deformation-dependent description. Consequently, shell effects are not dynamically incorporated into the potential energy surface and Q-values, but rather treated statically. To investigate how shell effects shape the detailed fragment yields, we extend the framework to include deformation-dependent masses and systematically explore their role in near-barrier MNT collisions.

Using this extended framework, we perform calculations for three carefully chosen systems designed to isolate the specific influence of the target's shell effects: ^{136}Xe + ^{208}Pb ($N = 126$), ^{204}Hg ($N = 124$), and ^{208}Hg ($N = 128$). The main improvement is the implementation of a deformation-dependent mass formula based on the Myers–Swiatecki mass prescription [40], with its parameters refitted to AME2020. A scaling factor a is further introduced to linearly vary the shell-correction strength, providing a controlled way to trace how shell effects influence the entire reaction sequence, from nucleon exchange to fragment survival after deexcitation.

2. Methods

This work extends the CLIM-H framework by employing a phenomenological nuclear mass formula that includes deformation-dependent shell corrections. The mass formula provides the nuclear masses needed at each stage of the calculation, thereby embedding shell effects self-consistently into the potential energy surface and Q-values for nucleon transfer. A shell scaling factor a is incorporated to linearly tune the strength of the shell correction. The following details how this deformation-dependent mass description is incorporated into the model's important components: the Langevin dynamics for shape evolution and the master equation for nucleon exchange.

The mass of a nucleus with given Z, N, and deformation $\xi(\mathbf{q})$, where $\mathbf{q}$ denotes the collective coordinates, is

$$M(Z,N;\xi(\mathbf{q})) = M_{\mathrm{mac}}(Z,N;\xi(\mathbf{q})) + aM_{\mathrm{mic}}(Z,N;\xi(\mathbf{q}))\exp(-E^*/E_d). \tag{1}$$

Here, $M_{\mathrm{mac}}(Z,N;\xi(\mathbf{q}))$ and $M_{\mathrm{mic}}(Z,N;\xi(\mathbf{q}))$ denote the macroscopic liquid-drop term and the microscopic shell correction, respectively. Both terms follow the analytical forms of Myers and Swiatecki [40,41] (specifically, Eq. (9) of Ref. [40] for the macroscopic part and Eq. (1) of Ref. [41] for the shell correction), with all parameters refitted to the AME2020 [39]. The refitted formula achieves a root-mean-square deviation of 1.46 MeV for nuclei with $A > 50$. The dimensionless scaling factor a allows us to linearly vary the strength of the shell correction: $a = 0$ corresponds to the macroscopic liquid-drop model (no shell effects), $a = 1$ to the realistic mass, and $a > 1$ to artificially amplified shell effects. The shell correction is attenuated by the factor $\exp(-E^*/E_d)$ to account for its damping with excitation energy E^*, following a treatment similar to Ref. [42], where E_d is the damping parameter. The excitation energy E^* of a fragment is taken as its share of the total dissipated energy, apportioned in proportion to its mass.

For shapes that are axially symmetric about the z-axis (beam direction), $\xi^2(\mathbf{q})$ is defined as a quantity proportional to the mean-square deviation of the nuclear surface from a sphere [43]:

$$\xi^2(\mathbf{q}) = \frac{1}{2}\int dz\big[r(z;\mathbf{q}) - R_0\big]^2 \sin\vartheta(z)\left|\frac{d\vartheta}{dz}\right|, \tag{2}$$

with $r(z;\mathbf{q})$ the distance from the symmetry axis to the surface, ϑ the polar angle in the cylindrical coordinate system, and $R_0 = 1.25A^{1/3}$ fm. This deformation-dependent mass formula allows us to compute the shell corrections of the collision system at any stage of its shape evolution.

In Eq. (1), $M_{\mathrm{mic}}(Z,N)$ is negative for doubly magic nuclei (e.g., ^{208}Pb), stabilizing spherical shapes, and positive for non-magic nuclei, favoring deformation. The masses from Eq. (1) are used to construct the system potential energy $V(\mathbf{q})$ and Q-values for nucleon transfer, ensuring that shell effects are propagated consistently through the reaction dynamics.

The shapes of the projectile-like fragment (PLF) and target-like fragment (TLF) within the reaction plane are modeled as circular arcs smoothly connected by a hyperbolic neck. The shape is parameterized by three collective coordinates: the center-to-center distance s, the neck-to-total volume ratio σ, and the radius asymmetry Δ. Crucially, for the assumed shapes, the radius asymmetry Δ is in one-to-one correspondence with the mass asymmetry $\alpha = (A_{\mathrm{P}} - A_{\mathrm{T}})/(A_{\mathrm{P}} + A_{\mathrm{T}})$, where A_{P} and A_{T} are the mass numbers of the PLF and TLF, respectively. Additionally, three rotational angles $(\theta_{\mathrm{P}}, \theta_{\mathrm{T}}, \theta)$ describe the intrinsic rotations of the fragments and the overall rotation.

The surface profile is described by a contour function $P(z;\mathbf{q})$. The distance $r(z;\mathbf{q})$ from the symmetry axis to the surface, as required in Eq. (2), is given by: for the PLF, $r^2(z;\mathbf{q}) = P^2(z;\mathbf{q}) + z^2$, and for the TLF, $r^2(z;\mathbf{q}) = P^2(z;\mathbf{q}) + (z - s)^2$.

In the CLIM-H framework, Δ is not evolved by the Langevin equations but is instead fixed at each time step by the mass asymmetry obtained from the master equation (Eq. (5)). The time evolution of the remaining coordinates $q_i = \{s, \sigma, \theta_{\mathrm{P}}, \theta_{\mathrm{T}}, \theta\}$ and their conjugate momenta p_i follows Langevin equations:

$$\begin{aligned} \dot{q}_i &= \sum_j [\boldsymbol{\mu}^{-1}(\mathbf{q})]_{ij} p_j, \\ \dot{p}_i &= -\frac{\partial}{\partial q_i}\big[T(\mathbf{p},\mathbf{q}) + V(\mathbf{q})\big] - \sum_j \big[R_{ij}(\mathbf{q})\dot{q}_j + g_{ij}(\mathbf{q})\Gamma_j(t)\big], \end{aligned} \tag{3}$$

where $\boldsymbol{\mu}(\mathbf{q})$ is the inertia tensor (calculated in the Werner-Wheeler approximation [44]), $T(\mathbf{p},\mathbf{q})$ the kinetic energy, and $V(\mathbf{q})$ the potential energy. The friction tensor $R_{ij}(\mathbf{q})$ originates from one-body dissipation [45], and the corresponding random-force amplitudes $g_{ij}(\mathbf{q})$ follow from the fluctuation-dissipation theorem [45,46], with $\Gamma_j(t)$ being a normalized white noise.

The potential energy $V(\mathbf{q})$, which is essential for analyzing shell effects, is

$$V(\mathbf{q}) = M_{\mathrm{P}}c^2 + M_{\mathrm{T}}c^2 + V_{12}(\mathbf{q}), \tag{4}$$

where $M_{\mathrm{P}} \equiv M(Z_{\mathrm{P}}, N_{\mathrm{P}}; \xi(\mathbf{q}))$ and $M_{\mathrm{T}} \equiv M(Z_{\mathrm{T}}, N_{\mathrm{T}}; \xi(\mathbf{q}))$ are the rest masses for the PLF and TLF, respectively, as given by Eq. (1) and thus contain the shell corrections. Here, Z_{P} and N_{P} (Z_{T} and N_{T}) denote the proton and neutron numbers of the PLF (TLF). $V_{12}(\mathbf{q})$ is the total interaction potential (nuclear plus Coulomb) obtained by double-folding the Yukawa-plus-exponential and Coulomb interactions [47,48], with parameters unchanged from Refs. [37,45].

Nucleon exchange is treated as a stochastic Markov process, described by a master equation for the probability $P_{(Z,N)}(t)$ of finding a fragment in state (Z, N) at time t:

$$\frac{\partial P_{(Z,N)}(t)}{\partial t} = \sum_{(Z_i,N_i)} \Lambda_{(Z_i,N_i)\to(Z,N)} P_{(Z_i,N_i)}(t) - \sum_{(Z_j,N_j)} \Lambda_{(Z,N)\to(Z_j,N_j)} P_{(Z,N)}(t), \tag{5}$$

The transition rate $\Lambda^{(a,b)}_{(Z,N)}(\mathbf{q}) = p^{(a,b)}_{(Z,N)}(\mathbf{q})/\tau$ corresponds to the transfer $(Z, N) \to (Z + a, N + b)$, where τ is a characteristic collision time [49]. The master equation is coupled self-consistently to the Langevin equations: at each time step, the nucleon numbers (Z, N) obtained from the master equation uniquely determine α; which, through the one-to-one correspondence $\alpha \leftrightarrow \Delta$, fixes the value of Δ that is then used in the Langevin evolution of the remaining collective coordinates.

The single-nucleon transfer probability $p^{(a,b)}_{(Z,N)}(\mathbf{q})$ depends on the Q-value:

$$p^{(a,b)}_{(Z,N)}(\mathbf{q}) = \frac{\exp\left\{-\left[\frac{Q^{(a,b)}_{(Z,N)}(\mathbf{q})-Q_{\rm opt}}{\hbar\omega_0}\right]^2\right\}}{1+\exp[2k(s-s_0)]}, \tag{6}$$

where $s_0 = 1.25(A_P^{1/3} + A_T^{1/3})$ fm, $\hbar\omega_0 = 1/\tau$, and $Q_{\rm opt}$ an optimum Q-value defined as in Ref. [37]. The wavenumber k is determined by the nucleon separation energies of the interacting fragments, calculated from the masses given by Eq. (1) following the method of Refs. [50,51].

The Q-value for a given transfer step is computed from the masses of the fragments. Since these masses are now obtained from the deformation-dependent formula of Eq. (1), the Q-value implicitly carries the information of shell corrections and their evolution with fragment shapes throughout the reaction. Shell corrections in the masses therefore directly determine the Q-value, which in turn influences the transfer probability via Eq. (6).

For the model implementation in this study, the primary cross sections are obtained by solving Eq. (3) coupled with Eq. (5) until the fragments separate ($s > 40$ fm). The same set of CLIM-H parameters is used for all calculations. The incident energy in the center-of-mass frame is set to $E_{\rm c.m.} = 1.066\ V_B$, where V_B denotes the Coulomb barrier of the corresponding system [52]. An ensemble of trajectories covering the orbital angular momentum range $l = 0$–$1000\ \hbar$ is simulated to account for the cross section. For each trajectory, after obtaining the primary fragment distribution from the CLIM-H calculation, statistical deexcitation is treated using the GEMINI$++$ code [53], which has been benchmarked against other deexcitation models in the heavy-mass region [54]. Final cross sections are obtained by summing over all trajectories after deexcitation.

3. Analysis and results

This work investigates how shell effects influence MNT dynamics to identify favorable collision partners for producing neutron-rich $N = 126$ nuclei. To isolate the role of the target's shell effects, we systematically compare three reactions — ^{136}Xe$+^{208}$Pb, ^{136}Xe$+^{204}$Hg, and ^{136}Xe$+^{208}$Hg. In each case, the same $N = 126$, $Z \leq 80$ isotope (e.g., ^{203}Ir) is chosen as the final product; although the proton and neutron compositions of the required transfer differ between targets, the total number of transferred nucleons is fixed for a given isotone. This reference point ensures that any difference in yield can be directly attributed to the target's shell effect.

The model is validated against experimental data for ^{136}Xe$+^{208}$Pb at $E_{\rm c.m.} = 450$ MeV ($\sim 1.066 V_B$) [55]. The impact of shell effects on the MNT yields is directly visualized in Fig. 1, which compares the experimental data (yellow circles) with calculations for $a = 1$ (red solid line) and $a = 0$ (black dashed line) across isotopic chains from tungsten ($Z = 74$) to lead ($Z = 82$).

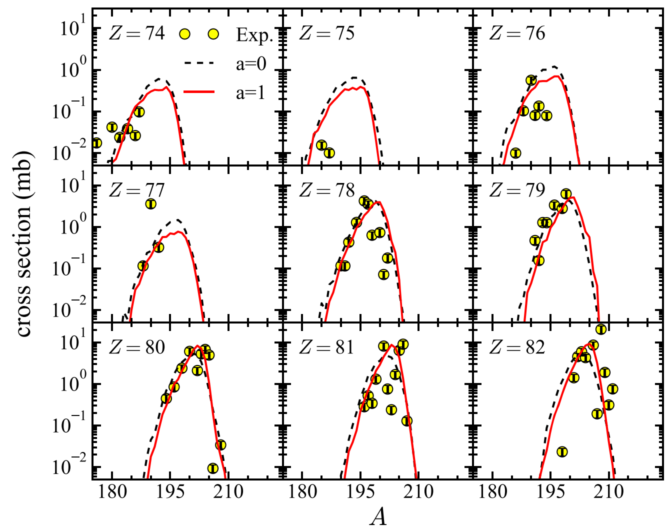

Fig. 1. Comparison of calculated and experimental [55] cross sections for the ^{136}Xe+^{208}Pb reaction at $E_{\rm c.m.} = 450$ MeV ($\simeq 1.066\ V_B$). Experimental data (yellow circles) are compared with CLIM-H predictions for $a = 0$ (black dashed line) and $a = 1$ (red solid line) final cross sections.

The model with realistic shell effects reproduces the main features of the measured isotopic distributions. For Pt ($Z = 78$) and Au ($Z = 79$), the predicted peak positions and distribution shapes agree well with the data. For lighter elements ($Z = 74 - 77$), where experimental cross sections are low (typically < 1 mb), the model provides a qualitative description. The deviations for the lighter elements are likely related to the sensitivity of the deexcitation process to the excitation energy deposited in the primary fragments, an aspect that still requires careful modeling.

A detailed comparison between the $a = 0$ and $a = 1$ calculations in Fig. 1 reveals the influence of shell corrections on the final yields. For isotopes near the entrance channel, the $a = 1$ results agree well with the data, whereas the $a = 0$ calculation underestimates the yields. In contrast, for multi-nucleon transfer products, $a = 0$ lies systematically above both $a = 1$ and the experimental data. This systematic trend is further corroborated by the mass distribution (Supplementary Fig. S1 [56]), where $a = 0$ overestimates the yields for $A \lesssim 200$ and $a = 1$ enhances the yields closer to the entrance channel. Thus, the realistic ($a = 1$) calculation captures the dual role of the shell effect: it enhances few-nucleon transfers while hindering multi-nucleon transfer channels.

To unravel the microscopic mechanism behind the dual role of shell effects, we examine nucleon exchange at characteristic stages of the collision. In heavy-ion collisions, large angular momentum leads to grazing collisions where few-nucleon transfer dominates, while smaller angular momentum leads to deeper contact where multinucleon transfer becomes more probable. We therefore adopt two characteristic configurations: for few-nucleon transfer, a grazing configuration ($s \approx 1.25(A_P^{1/3} + A_T^{1/3}) + 0.5$ fm, $\sigma = 0$); for multinucleon transfer, a more compact configuration corresponding to the distance of dynamical closest approach ($s \approx 13$ fm, $\sigma \approx 0.05$ for the systems studied here). To quantify the probability of reaching a given fragment (Z, N) from the initial collision partner (Z_0, N_0) under these conditions, we introduce the cumulative transfer probability $P_{\rm cum}$, defined as the maximum possible probability along a hypothetical stepwise transfer path during a single passage through the relevant region:

$$P_{\rm cum} = \max_{\text{all paths}} \left[\prod_{k=1}^{n} p^{(\Delta Z_k, \Delta N_k)}_{(Z_{k-1},N_{k-1})}\right], \tag{7}$$

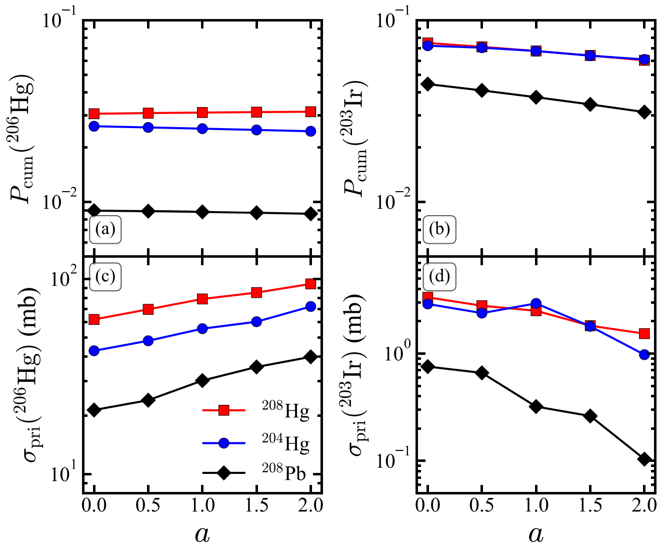

Fig. 2. $P_{\rm cum}$ (a, b) and primary cross section $\sigma_{\rm pri}$ (c, d) for ^{206}Hg (left panels) and ^{203}Ir (right panels) versus the scaling factor a, for collisions of ^{136}Xe with ^{208}Pb (black diamonds), ^{204}Hg (blue circles), and ^{208}Hg (red squares). The lines are guides to the eye.

where n is the total number of transfer steps, and $(\Delta Z_k, \Delta N_k)$ represents the nucleons transferred in the kth step.

Using the shell scaling factor a as a controlled variable, we can trace how shell corrections influence each step of the nucleon exchange. By linearly varying a (taking values 0, 0.5, 1, 1.5, 2), we systematically alter the shell correction strength from zero to an enhanced value ($a > 1$). This allows us to quantify how $P_{\rm cum}$ for specific products evolves with a, thereby disentangling the influence of the shell effect on the MNT dynamics.

Fig. 2(a) and (b) display $P_{\rm cum}$ for ^{206}Hg and ^{203}Ir, respectively, across the three systems, revealing a striking contrast. For ^{206}Hg (Fig. 2(a)), which requires only a two-nucleon transfer, $P_{\rm cum}$ remains nearly constant or even increases slightly with a. This indicates that shell effects do not hinder few-nucleon transfer near the entrance channel, and may even facilitate it for ^{208}Hg. In sharp contrast, $P_{\rm cum}$ for ^{203}Ir (Fig. 2(b)), a five-nucleon transfer product, decreases markedly as a increases, with the strongest suppression occurring for the double-magic ^{208}Pb target. This trend directly shows how enhanced shell effects inhibit the incremental probability of forming a nucleus that requires a large transferred nucleon.

The consequences of this microscopic effect are reflected in the primary cross sections $\sigma_{\rm pri}$ (Fig. 2(c) and (d)). For ^{206}Hg, $\sigma_{\rm pri}$ rises with a, owing mainly to the reduction in the required transferred nucleon. Conversely, for ^{203}Ir, $\sigma_{\rm pri}$ drops sharply with increasing a, most dramatically for ^{208}Pb. The close correspondence between the $P_{\rm cum}$ and $\sigma_{\rm pri}$ trends establishes a clear cause-and-effect link: shell-induced suppression of the microscopic transfer probability is the key mechanism that drastically reduces the macroscopic yield of multi-nucleon transfer channels. We note that the increase of $P_{\rm cum}$ for ^{206}Hg is less pronounced than that of $\sigma_{\rm pri}$. This is likely because some ^{206}Hg are produced during close contact between the colliding partners, where the transfer paths differ from the typical grazing trajectory used in the $P_{\rm cum}$ calculation.

The scaling of a reveals that the cumulative inhibition of successive transfer probabilities underlies the macroscopic yields. For few-nucleon transfer (^{206}Hg), the weak variation of $P_{\rm cum}$ allows $\sigma_{\rm pri}$ to rise as the transferred nucleon decreases. For multi-nucleon transfer (^{203}Ir), the strong suppression of $P_{\rm cum}$ with a directly drives the sharp drop in $\sigma_{\rm pri}$. This demonstrates that the decrease of multi-nucleon transfer yields originates from the reduction of $P_{\rm cum}$: for a stabilized target, larger a means greater resistance to nucleon transfer, which lowers the cumulative transfer probability and in turn reduces $\sigma_{\rm pri}$. This effect is most pronounced for the doubly magic ^{208}Pb.

The above analysis shows that shell effects, encoded in the scaling factor a, govern primary fragment production by affecting microscopic transfer probabilities. The experimentally observable cross sections, however, are obtained only after statistical deexcitation. To assess the shell effect's full impact on observable yields, we now examine how it influences fragment survival. For each system and each value of a, we compare the primary ($\sigma_{\rm pri}$) and final ($\sigma_{\rm fin}$) cross sections and define the survival ratio $R(a) = \sigma_{\rm fin}(a)/\sigma_{\rm pri}(a)$, which represents the fraction of primary fragments that survive deexcitation. In the neutron-rich $N = 126$ region, one typically finds $R(a) < 1$, reflecting deexcitation losses.

The scaling factor a does not alter the nuclear input parameters (e.g., level densities and decay widths) employed internally by GEMINI++. However, it affects the reaction dynamics within CLIM-H, thereby changing the excitation energy and angular momentum distributions of the primary fragments. This leads to an a-dependent survival ratio $R(a)$.

Fig. 3 shows $R(a)$ for ^{206}Hg and ^{203}Ir. The behavior differs markedly between the two nuclei. For ^{206}Hg (Fig. 3(a)), R remains close to 1, indicating that primary fragments have relatively low average excitation. In ^{136}Xe + ^{208}Hg, R is closest to 1 for all a, due to feeding from the deexcitation of more neutron-rich primary isotopes (e.g., ^{207,208}Hg → ^{206}Hg).

For ^{203}Ir, R is significantly lower ($R < 0.2$) and drops steeply with increasing a. The suppression is most pronounced for ^{136}Xe +^{208} Pb, where R falls most dramatically with a. This indicates that primary ^{203}Ir fragments are typically highly excited, and their excitation increases substantially when shell effects are enhanced, making them unlikely to survive deexcitation.

Taking the ^{208}Pb target, where the shell effect is strongest, the final cross section of ^{203}Ir can be decomposed into primary-production and survival contributions. The shell correction reduces the primary yield by only ≈ 16%, while the survival probability drops by a factor of ≈ 3. Since the deexcitation code is identical in both cases, this large change in survival must originate from the different primary fragment distributions and their internal configurations produced with and without shell corrections. At $a = 0$, the absence of shell effects permits the transfer of more nucleons in the multi-nucleon transfer channels; these primary fragments carry higher internal excitation, and their subsequent nucleon evaporation feeds the ^{203}Ir channel, enhancing the final yield. As shown in the total kinetic energy loss (TKEL) distribution (Supplementary Fig. S2 [56]), the shell correction shifts the spectrum toward lower TKEL values, indicating that the primary fragments are indeed less excited. The shell effect thus influences the final yields primarily through the dynamical stage, by modifying both the transfer paths and the excitation energy of the primary fragments; the corresponding change in the survival ratio is a consequence of these dynamical differences, rather than an independent effect originating in the deexcitation stage.

This mechanism also explains the systematic target dependence of the survival ratio. For ^{206}Hg, a few-nucleon transfer product, R is close to unity for all targets and is highest for $N > 126$ targets because primary fragments with a neutron excess preferentially evaporate neutrons, feeding the final yield toward the $N = 126$ shell. For ^{203}Ir, in contrast, the survival probability is systematically higher with the non-magic Hg targets than with the double-magic ^{208}Pb. The magic target not only suppresses multi-nucleon transfer dynamically (Fig. 2), but compared to non-magic targets, each transferred nucleon from a doubly magic target deposits more excitation energy into the primary fragments, further diminishing their survival. The combination of these two effects makes doubly magic targets particularly unfavorable for producing neutron-rich $N = 126$ nuclei.

The insights gained above, which suggest avoiding magic nuclei as collision partners and favoring neutron-rich non-magic ones, allow us to propose a more optimized reaction system. We consider ^{238}U+^{204}Hg at $E_{\rm c.m.} \simeq 1.45\ V_B$. Previous work [38] has shown that $E_{\rm c.m.} \simeq (1.4–1.6)$

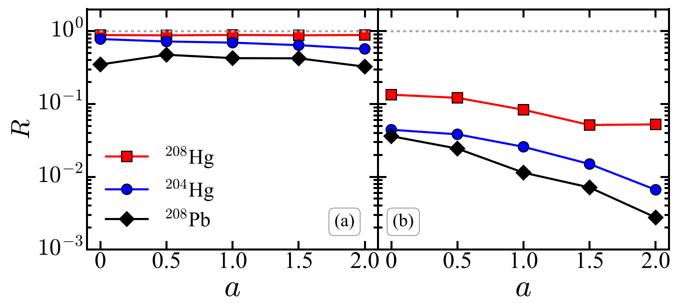

Fig. 3. Survival ratio R for ^{206}Hg (a) and ^{203}Ir (b) as a function of the scaling factor a for collisions of ^{136}Xe with ^{208}Pb (black diamonds), ^{204}Hg (blue circles), and ^{208}Hg (red squares). The horizontal dashed line at $R = 1$ serves as a visual reference. The lines are guides to the eye.

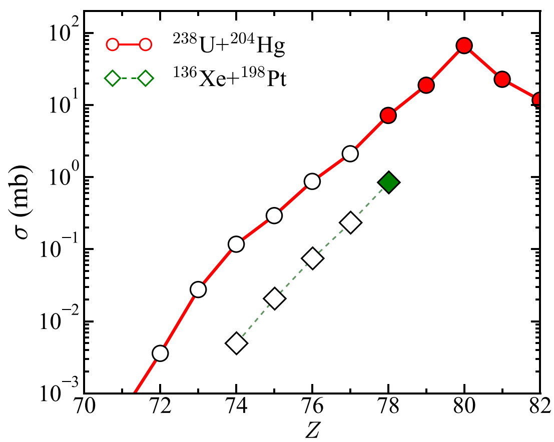

Fig. 4. Predicted final cross sections for $N = 126$ isotones produced in ^{238}U+^{204}Hg at $E_{\text{c.m.}} \simeq 1.45V_B$ (red solid line and circles, with open symbols indicating isotones with as-yet unknown ground-state properties), compared with experimental data for ^{136}Xe+^{198}Pt at $E_{\text{c.m.}} \simeq 1.6V_B$ (green dashed line and diamonds) [18]. The lines are guides to the eye.

V_B favors producing neutron-rich $N = 126$ nuclides in such systems. We choose $E_{\text{c.m.}} = 1.45V_B$, which optimally balances the transfer and survival: higher energy reduces the distance of closest approach, enhancing P_{cum}, but also increases fragment excitation energy, which can dampen shell effects and reduce R. At 1.45 V_B, P_{cum} is sufficiently high while the excitation energy deposited in the TLF remains moderate (because the ^{204}Hg-like fragments are lighter than the ^{238}U-like fragments), so shell corrections stay effective and R does not drop sharply. Thus, this energy makes ^{238}U+^{204}Hg a favorable system for producing exotic $N = 126$ isotones.

Fig. 4 displays the predicted final cross sections for $N = 126$ isotones produced in the ^{238}U +^{204} Hg reaction (red circles). The yields rise smoothly with Z, approaching 100 mb for ^{206}Hg. Notably, even for the relatively light isotone at $Z = 72$ (^{198}Hf), the predicted final cross section remains as high as $\sim 3.6\ \mu$b. For the neutron-rich isotopes ^{203}Ir and ^{202}Os, the calculated final cross sections are 2.1 mb and 0.87 mb, respectively. For comparison, the experimental yields for the benchmark system ^{136}Xe+^{198}Pt at $E_{\text{c.m.}} \simeq 1.6\ V_B$ are also included [18].

4. Conclusion

This study elucidates how shell effects influence the synthesis of neutron-rich nuclei near $N = 126$ in multinucleon transfer reactions. By extending the CLIM-H model with a deformation-dependent mass formula and introducing a scaling factor a, we systematically traced the influence of the shell effect on the reaction dynamics. The analysis reveals a dual role of shell effects: they enhance the production of fragments close to the entrance-channel configuration while strongly suppressing those that require a large number of transferred nucleons. This suppression is most pronounced for double-magic targets such as ^{208}Pb, making them inefficient for producing neutron-rich isotopes of interest like ^{203}Ir.

The microscopic mechanism underlying this suppression is identified through the cumulative transfer probability P_{cum}: enhanced shell corrections progressively inhibit P_{cum} along the optimal path to a multinucleon transfer product, which in turn reduces the primary cross section σ_{pri}. The same shell effects also modify the excitation energy of the primary fragments: compared to non-magic targets, each nucleon transferred from a doubly magic target deposits more excitation energy, further reducing the survival probability during statistical deexcitation.

Our results provide clear guidance for selecting reaction partners to produce neutron-rich $N = 126$ nuclei: closed shell nuclei like doubly magic ^{208}Pb should be avoided, as they suppress multi-nucleon transfer channels in the reaction dynamics, and the associated increase in fragment excitation energy further reduces survival during deexcitation. While focused on $N = 126$, this principle likely holds for other magic numbers. A concrete example is the ^{238}U+^{204}Hg at $E_{\text{c.m.}} \simeq 1.45V_B$, which is predicted to yield final cross sections of 2.1 mb and 0.87 mb for ^{203}Ir and ^{202}Os, respectively. Looking forward, the use of neutron-rich radioactive ion beams would further maximize the production of these rare isotopes by fully leveraging the dynamical and deexcitation advantages identified in this work.

Data availability

Data will be made available on request.

Declaration of competing interest

The authors declare that they have no known competing financial interests or personal relationships that could have appeared to influence the work reported in this paper.

Acknowledgments

The authors are grateful to Dr. Y. J. Feng for valuable discussions and assistance with this work. This work was supported by the Strategic Priority Research Program of the Chinese Academy of Sciences (Grant No. XDB34010300), the National Key R&D Program of China (Grant Nos. 2023YFA1606404, 2024YFE0109804, 2022YFA1602302, 2023YFA1606402), the National Natural Science Foundation of China (Grants Nos. 12475127, 12375130, 12022501, 12235020, 12561160119), the Dean's Foundation of China Institute of Atomic Energy (Grant No. 12YZ010270624219), the CAS Project for Young Scientists in Basic Research (Grant No. YSBR-002), the Research Program of Heavy Ion Science and Technology Key Laboratory, Institute of Modern Physics, Chinese Academy of Sciences (Grant Nos. HIST2024KS04, HIST2024CO04), the Longyuan Youth Innovation and Entrepreneurship Talent Project of Gansu Province (Grant No. 24GD13GA005), and Science and Technology Major Project of Gansu Province (Grant No. 2024GZT04).

Supplementary material

Supplementary material associated with this article can be found in the online version at 10.1016/j.physletb.2026.140614.

References

[1] G.G. Kiss, Z. Podolyák, Eur. Phys. J. A 60 (9) (2024) 175.
[2] T.T. Yeung, et al., Phys. Rev. Lett. 133 (2024) 072501.
[3] X.Y. Wu, J.M. Yao, Phys. Rev. C 99 (2019) 054329.
[4] H. Grawe, K. Langanke, G. Martínez-Pinedo, Rep. Prog. Phys. 70 (9) (2007) 1525.

[5] J.J. Cowan, et al., Rev. Mod. Phys. 93 (2021) 015002.
[6] E.M. Holmbeck, T.M. Sprouse, M.R. Mumpower, Eur. Phys. J. A 59 (2) (2023) 28.
[7] B. Liu, Doctoral Dissertation, 2025.
[8] M. Li, G.C. McLaughlin, R. Surman, Phys. Lett. B 872 (2026) 140109.
[9] A.I. Morales, et al., Phys. Rev. Lett. 113 (2014) 022702.
[10] J.-L. You, Q.-D. Wu, X.-P. Zhang, Q.J. Zhi, Commun. Theor. Phys. 71 (3) (2019) 293.
[11] W.M. Seif, A. Adel, Phys. Rev. C 113 (2026) 034304.
[12] S. Rosswog, O. Korobkin, A. Arcones, F.-K. Thielemann, T. Piran, Mon. Not. R. Astron. Soc. 439 (1) (2014) 744–756.
[13] G.G. Adamian, N.V. Antonenko, A. Diaz-Torres, S. Heinz, Eur. Phys. J. A 56 (2) (2020) 47.
[14] S. Heinz, H.M. Devaraja, Eur. Phys. J. A 58 (6) (2022) 114.
[15] Z.-Q. Feng, Phys. Rev. C 95 (2017) 024615.
[16] K. Zhao, Z. Liu, F. Zhang, N. Wang, Phys. Lett. B 815 (2021) 136101.
[17] Z. Liao, L. Zhu, J. Su, C. Li, Phys. Rev. C 107 (2023) 014614.
[18] Y.X. Watanabe, et al., Phys. Rev. Lett. 115 (2015) 172503.
[19] I.V. Vorobiev, et al., Phys. Rev. C 112 (2025) 014625.
[20] E.M. Kozulin, et al., Phys. Rev. C 109 (2024) 034616.
[21] H. Devaraja, et al., Phys. Lett. B 862 (2025) 139353.
[22] Y. Zou, M.-H. Zhang, M.-C. Wang, Y.-H. Zhang, F.S. Zhang, Nucl. Sci. Tech. 35 (10) (2024) 180.
[23] V.V. Saiko, A.V. Karpov, Phys. Rev. C 112 (2025) 064609.
[24] G.G. Adamian, N.V. Antonenko, A.S. Zubov, Phys. Rev. C 71 (2005) 034603.
[25] G. Zhang, F.S. Zhang, Phys. Rev. C 111 (2025) 014603.
[26] Z. Shen, Z. Liao, L. Zhu, Phys. Rev. C 113 (2026) L021601.
[27] Y. Feng, Y. Huang, E. Xiao, X. Lei, L. Zhu, J. Su, Phys. Rev. C 107 (2023) 044606.
[28] Y. Feng, et al., Phys. Rev. C 109 (2024) 054604.
[29] K. Sekizawa, K. Yabana, Phys. Rev. C 93 (2016) 054616.
[30] Z. Wu, X. Sun, L. Guo, Phys. Rev. C 113 (2026) 024618.
[31] S. Ayik, M. Arik, E. Erbayri, O. Yilmaz, A.S. Umar, Phys. Rev. C 108 (2023) 054605.
[32] D.D. Zhang, D. Vretenar, T. Nikšić, P.W. Zhao, J. Meng, Phys. Lett. B 869 (2026) 139828.
[33] K. Hildenbrand, et al., Nucl. Phys. A 405 (1) (1983) 179–204.
[34] G. Guarino, et al., Nucl. Phys. A 424 (1) (1984) 157–183.
[35] P. Gippner, et al., Z. Phys. A. At. Nucl. 325 (3) (1986) 335–346.
[36] A. Türler, et al., Phys. Rev. C 46 (1992) 1364–1382.
[37] F.C. Dai, et al., Phys. Rev. C 109 (2024) 024617.
[38] F.C. Dai, et al., Phys. Rev. C 112 (2025) 014621.
[39] M. Wang, W.J. Huang, F.G. Kondev, G. Audi, S. Naimi, Chin. Phys. C 45 (2021) 030003.
[40] W. Myers, W. Swiatecki, Nucl. Phys. 81 (2) (1966) 1–60.
[41] W. Myers, W. Swiatecki, Anomalies in Nuclear Masses, Tech. rep.
[42] L. Zhu, et al., Phys. Rev. C 97 (2018) 044614.
[43] J. Blocki, O. Mazonka, J. Wilczynski, Z. Sosin, A. Wieloch, Acta Phys. Pol. B 31 (7) (2000) 1513.
[44] K.T.R. Davies, A.J. Sierk, J.R. Nix, Phys. Rev. C 13 (1976) 2385.
[45] H. Feldmeier, Rep. Prog. Phys. 50 (8) (1987) 915.
[46] L.-L. Liu, X.-Z. Wu, Y.-J. Chen, C.-W. Shen, Z.-X. Li, Z.G. Ge, Phys. Rev. C 99 (2019) 044614.
[47] H.J. Krappe, J.R. Nix, A.J. Sierk, Phys. Rev. C 20 (1979) 992–1013.
[48] P. Möller, J. Nix, Nucl. Phys. A 361 (1) (1981) 117–146.
[49] V.I. Zagrebaev, Phys. Rev. C 67 (2003) 061601.
[50] A. Winther, Nucl. Phys. A 572 (1) (1994) 191–235.
[51] A. Winther, Nucl. Phys. A 594 (2) (1995) 203–245.
[52] P.W. Wen, et al., 034606, Phys. Rev. C 105 (2022). 034606
[53] D. Mancusi, R.J. Charity, J. Cugnon, Phys. Rev. C 82 (2010) 044610.
[54] Y.X. Diao, Q.Q. Yao, T.L. Zhao, X.J. Bao, Phys. Rev. C 112 (2025) 064612.
[55] J.S. Barrett, et al., Phys. Rev. C 91 (2015) 064615.
[56] See supplemental material for the mass distribution (Fig. S1) and the TKEL distribution (Fig. S2).